Adjustments and Uncertainty Quantification for SLS Aerodynamic Sectional Loads

Derek J. Dalle*, Stuart E. Rogers†,
NASA Ames Research Center, Moffett Field, CA 94035

Henry C. Lee‡, and Jamie G. Meeroff§
Science and Technology Corp., Moffett Field, CA 94035

This paper presents a method for adjusting sectional loads to match target values for integrated force and moment coefficients. In a typical application, the sectional load profile for one flight condition is calculated from Computational Fluid Dynamics (CFD) while the integrated forces and moments are measured in a wind tunnel experiment. These two methods do not generally result in identical predictions, and this leads to an inherent inconsistency between different data products. This paper aims to provide a procedure to remove that inconsistency. A sectional load profile for a launch vehicle splits the rocket into slices along its length and calculates the aerodynamic loading on each slice, which leads to a one-dimensional aerodynamic load profile that is used for structural analysis. Adjusting sectional loads, also known as line loads, is a nontrivial matter due to several consistency constraints. For example, the adjusted sectional normal force profile must be consistent with both the integrated normal force and pitching moment. To avoid such inconsistency issues, this paper presents a method using a Proper Orthogonal Decomposition (POD) to generate basis functions to adjust the sectional load profiles. As a corollary, this correction method enables the creation of an uncertainty quantification for sectional loads that is consistent with the dispersed integrated force and moment database and its uncertainty quantification. Several extensions to this technique, such as applying the method to the surface pressures, are considered.

Nomenclature

C_A	=	*CA*, Axial force coefficient, body axis	c_m	=	Sectional load profile for *CLM*
C_N	=	*CN*, Normal force coefficient, body axis	c_N	=	Sectional load profile for *CN*
C_Y	=	*CY*, Side force coefficient, body axis	w_k	=	Objective function weight for ϕ_k
C_ℓ	=	*CLL*, Rolling moment coefficient	x	=	Axial coordinate [m]
C_m	=	*CLM*, Pitching moment coefficient	$\hat{x}$	=	Nondimensional coordinate, x/L_{ref}
C_n	=	*CLN*, Yawing moment coefficient	α	=	*alpha*, Angle of attack of the core
$\bar{C}_n$	=	Target value for C_n, e.g. from wind tunnel	β	=	*beta*, Angle of sideslip of the core
L_{ref}	=	Reference length [m]	ε_{CN}	=	Random dispersion for *CN*, in $[-1, 1]$
M	=	Flight Mach number	λ	=	Langrange multiplier
U_{CN}	=	Uncertainty in integrated *CN*	$\phi_{N,k}$	=	Sectional load adjustment k for *CN*
a_k	=	Coefficient for ϕ_k	σ	=	Singular value from SVD

*Aerospace Eng., Computational Aerosciences Branch, Member AIAA, derek.j.dalle@nasa.gov
†Aerospace Eng., Computational Aerosciences Branch, Associate Fellow AIAA, stuart.e.rogers@nasa.gov
‡Research Scientist/Eng., Computational Aerosciences Branch, Member AIAA, henry.c.lee@nasa.gov
§Research Scientist/Eng., Computational Aerosciences Branch, Member AIAA, jamie.g.meeroff@nasa.gov

Abbreviations

BMC	=	Balance Moment Center	POD	=	Proper Orthogonal Decomposition
CFD	=	Computational Fluid Dynamics	RSRB	=	Right-hand Solid Rocket Booster
cg	=	Center of gravity/mass	SLS	=	Space Launch System
LSRB	=	Left-hand Solid Rocket Booster	SRB	=	Solid Rocket Booster
MRP	=	Moment Reference Point	SVD	=	Singular Value Decomposition

I. Introduction

Aerodynamic sectional load profiles, also called line loads, are used for vehicle-scale structural analysis. The primary way in which this works is that the outer mold line of the vehicle is divided into many slices, which all have boundaries at fixed x-coordinates, and then to integrate the aerodynamic forces on each of these slices individually. Two images of these slices are shown below using the crewed configuration of NASA's Space Launch System Block 1B vehicle. Figure 1 shows the slices for the full vehicle and Fig. 2 focuses on just the forward portion of the same image. The directions of the coordinate axes are shown in Figs. 1 and 2, but the actual location of the origin is a point directly in front of the vehicle nose.

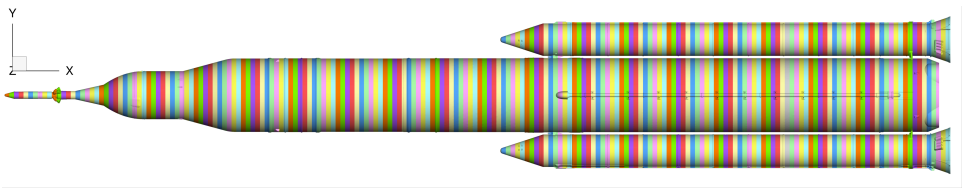

Figure 1. Sectional load slices for SLS Block 1B configuration

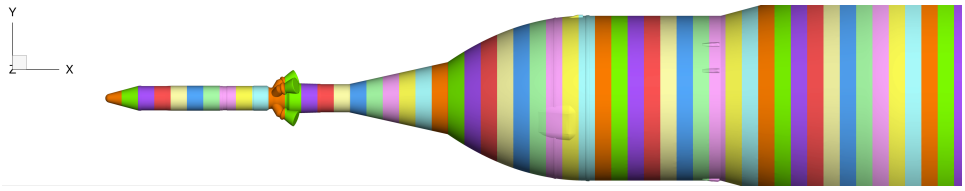

Figure 2. Sectional load slices on forward portion of SLS Block 1B configuration

In this work, sectional loads are extracted from Computational Fluid Dynamics (CFD) surface flow solutions [1]. The CFD solutions were obtained using either OVERFLOW 2.2L [2] or FUN3D 13.1 [3]. The actual calculation of sectional loads from the extracted surface solutions is performed using the utility *triload* [1], which is part of Chimera Grid Tools [4].

By storing the aerodynamic loads on each of these vehicle segments, the sectional load profile provides a representation of the vehicle as a line with forces in each of the three directions provided as functions along the length of that line. This enables structural analysis on the full scale of the vehicle provided that picking a primary axis like this is a valid assumption. These can be used to calculate the maximum load on the vehicle for a complete flight envelope, or it can be used as an input for aeroelastic bending analysis.

Because of the high resolution of data, the most common source for aerodynamic sectional load data is CFD. Before CFD was a practical choice, coarser sectional loads were measured using as many static pressure taps as a wind tunnel model could fit. Pressure-sensitive paint [5–7] is a developing alternative that uses experimental wind tunnel data

However, due to the long and well-tested history of using wind tunnels to develop force & moment databases, it is frequently the case that the sectional loads come from CFD while the integrated forces & moments come from a wind tunnel experiment. As a result, even if the two data sources are as similar as possible, there will be inconsistencies between the force & moment database and the forces one would

get by integrating the sectional loads. In realistic applications this is further complicated by differences in modeling such as geometric fidelity to the flight vehicle, Reynolds number, effects of wind tunnel walls, presence of a sting in the wind tunnel (but not in the CFD), and physical effects that are difficult to include in the wind-tunnel model, such as engine exhaust plumes.

This paper presents a method for adjusting the sectional loads (whatever the data source) so that when integrated along the length of the vehicle, they are consistent with the force & moment database. This sounds like a relatively trivial process, but in practice turns out to have several difficulties. For example, if the wind tunnel normal force coefficient for a case at zero angle of attack is 0.01 and the CFD normal force for the same conditions is −0.01, a simple scaling of the load profile results in flipping the entire profile. Even worse adjustments occur if the CFD normal force coefficient is 0.001 with a wind tunnel measurement of 0.02. Figure 3 shows an example of this anomaly using the actual SLS Block 1B normal force profile at Mach 1.75, zero degrees angle of attack, and zero sideslip.

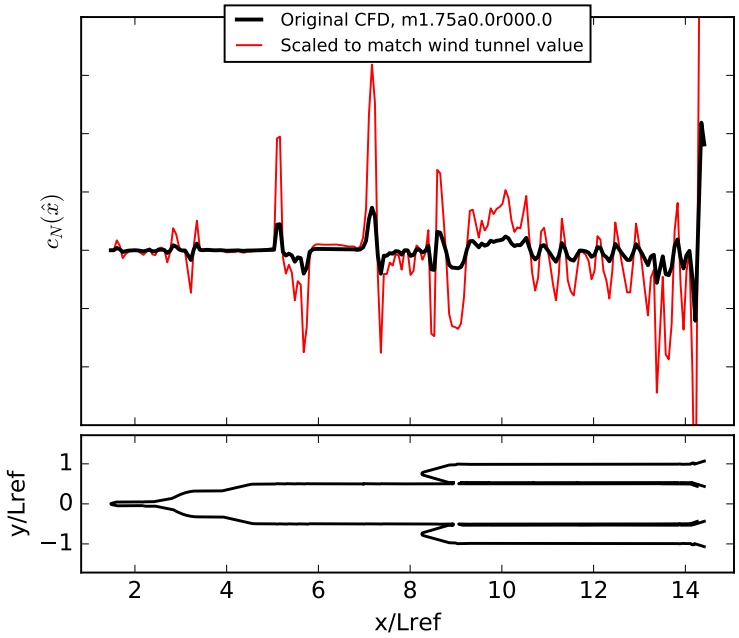

Figure 3. Directly scaled *CN* profile for Mach 1.75, zero angle of attack and zero sideslip

Large local loads like those seen in the peaks of the red curve in Fig. 3 are harmful to launch vehicle because they determine how strong the launch vehicle needs to be. An artificially high (in magnitude) line load profile will result in an unnecessarily strong vehicle structural, and the extra weight needed to make this stiff structure may decrease the useful payload to orbit, the Moon, or wherever the eventual destination of the vehicle may be.

Although both the CFD and the wind tunnel predict small values of *CN* for this condition, the wind tunnel value is about five times larger. As a result the directly scaled red profile in Fig. 3 is very large. Although the numerical values of the load profile are withheld here, the local loads resulting from this scaling are large even compared to the results at ±4° angle of attack.

Furthermore, there need to be at least two degrees of freedom to the adjustment to ensure that integrating the sectional loads is consistent with the database for both a force and a moment coefficient at every flight condition. A typical example with two degrees of freedom uses a linear combination of two terms: a constant offset, and a linear offset function. This approach has some of the same problems from the previous paragraph and further does not address the issue that it inherently attempts to apply the same magnitude of correction to the nose and its very small cross-sectional area as it does to sections where the cross-sectional

area is much larger. Applying these kinds of offsets will also shift all the points at which the sectional load profile crosses zero, even though such locations are typically tied to physical features of the vehicle.

A robust and well-anchored adjustment method must utilize information about the typical size of the sectional load at each station and how robust the data is at each station. The method must do this automatically to avoid mistakes and/or biases by the user creating the adjustments. This paper proposes a robust adjustment method that utilizes a Proper Orthogonal Decomposition (POD) [8] with the sectional loads from neighboring cases as the input snapshots. This automatically creates candidate adjustment functions with features that are shared among the input snapshots. The POD provides more than the required two adjustment functions (specifically, it provides up to as many as the number of snapshots used to create the POD). An optimization technique is introduced to select the best linear combination to satisfy the consistency constraints. Broadly speaking, basis functions with large local adjustment magnitudes are disfavored, and basis functions with high singular values are favored for this optimization approach.

This approach can be generalized to a wide variety of problems with varying degrees of similarity to this one. For example, one could use the entire surface pressure solution from CFD as the snapshots and then perform a similar adjustment that simultaneously matches all three integrated forces and three integrated moments. It could also be used as a way to ensure that the CFD matches exactly pressures measured at specific points, much the way that is done in [9]. The proposed technique also enables an uncertainty quantification method for sectional loads which allows an engineer to propagate uncertainty in the integrated forces and moments back into the sectional loads.

The paper discusses the details of the proposed method II, and then provides some examples from actual design and development studies of NASA's Space Launch System in Sections III and IV. The numbers on the y-axes of most plots have been removed because the vehicle is currently under development. The use of a complex and realistic configuration for these examples is meant to demonstrate the robustness of the proposed method and its readiness for technical use within the industry.

II. Sectional Loads Adjustments

A sectional load database consists of a set of six sectional load profiles at each flight condition, three sectional force profiles and three sectional moment profiles. A flight condition is a combination of flight Mach number (M), altitude (h), angle of attack (α), and angle of sideslip (β). Reynolds number and temperature (or any other pair of variables that together define the dimensional freestream density and temperature) are also a critical part of the flight condition, but for launch vehicles, these parameters often follow a fixed schedule that is determined by Mach number. There are alternative methods to discretize a launch vehicle aerodynamic database, but the choice of flight conditions does not qualitatively affect this discussion of sectional loads.

At each flight condition (M, α, β), there is an integrated normal force coefficient C_N (also written CN) along with a sectional load profile $c_N(x)$ that gives the distribution of how this normal force is distributed along the length of the vehicle. The pitching moment C_m (also written CLM, with the L meaning "little") and pitching moment sectional profile $c_m(x)$ are similarly defined.

$$C_N = C_N(M, \alpha, \beta) \qquad c_N = c_N(x, M, \alpha, \beta) \tag{1}$$

$$C_m = C_m(M, \alpha, \beta) \qquad c_m = c_m(x, M, \alpha, \beta) \tag{2}$$

The sectional loads must integrate to be equal to the integrated loads. If x_1 is the coordinate of the nose of the vehicle, and x_2 is the coordinate of the tail, the integration consistency constraints can be written as follows.

$$C_N = \int_{x_1}^{x_2} c_N(x)\,\mathrm{d}x \qquad C_m = \int_{x_1}^{x_2} c_m(x)\,\mathrm{d}x \tag{3}$$

Furthermore, there is a relationship between the sectional normal force and pitching moment distributions. If the moments are calculated about a moment reference point x_{MRP}.

$$c_m(x) = \frac{x - x_{MRP}}{L_{ref}} c_N(x) \tag{4}$$

Typically these equations are written with a slight change in order to nondimensionalize the axial coordinate x by replacing it with $\hat{x}$=x/L_{ref}.

$$c_m(\hat{x}) = (\hat{x} - \hat{x}_{MRP}) c_N(\hat{x}) \tag{5}$$

$$C_N = \int_{\hat{x}_1}^{\hat{x}_2} c_N(\hat{x})\, \mathrm{d}\hat{x} \tag{6}$$

$$C_m = \int_{\hat{x}_1}^{\hat{x}_2} (\hat{x} - \hat{x}_{MRP}) c_N(\hat{x})\, \mathrm{d}\hat{x} \tag{7}$$

A similar relationship exists between the side force (C_Y or CY) and yawing moment (C_n or CLN), while the axial force (C_A or CA) and rolling moment (C_ℓ or CLL) are independent.

Consistency issues arise when the sectional load profile and integrated loads are calculated or measured using different methods. Typically this means the sectional load c_N is calculated using CFD while the integrated force $\bar{C}_N$ is measured during a wind tunnel test. However, there are other possibilities, such as using Pressure Sensitive Paint to generate the sectional load database. As a result, it will likely be the case that the constraints of both Eqs. (6) and (7) will be violated. In order to fix these inconsistencies, we add a correction function $\phi_N(\hat{x})$, so that

$$\bar{c}_N(\hat{x}) = c_N(\hat{x}) + a\phi_N(\hat{x}) \tag{8}$$

where a is just a constant that is selected by some means.

A. Methods That Do Not Work

To understand the new approach, it is worthwhile to look at how some simpler techniques fail. The first approach is use $\phi_N = c_N$, which is equivalent to scaling the original sectional normal force. In order to satisfy the integrated normal force constraint, Eq. (6), the solution would be

$$a = \frac{\bar{C}_N}{C_N} - 1$$

Even if this correction by coincidence also satisfied the pitching-moment constraint Eq. (7), this correction has significant problems when the normal force is close to zero. For flight conditions at zero degrees angle of attack, which is typically an important region of a launch vehicle's flight envelope, the integrated values for C_N are identically zero, or very close to zero. However, slight asymmetries in the vehicle such as a camera or similar feature may give a nonzero $c_N(x)$ value at a particular value of x. This may result in large changes in the sectional loads despite small errors in the integrated C_N, perhaps even replacing all positive values of c_N with negative values of $\bar{c}_N$.

A similar approach that also has insurmountable issues is to use a constant for the correction.

$$\phi_N(\hat{x}) = \frac{1}{\hat{x}_2 - \hat{x}_1}$$

Then setting $\bar{c}_N(\hat{x}) = c_N(\hat{x}) + a\phi_N(\hat{x})$, we can find that the correction magnitude is

$$a = \bar{C}_N - C_N$$

This correction at least does not have the potential to reduce the entire sectional load profile; instead it distributes the correction evenly across the length of the rocket. However, this still has some lesser issues. For example, there may be sections of the vehicle for which c_N really should be zero, and this correction shifts all such regions to a small nonzero value. In addition, this type of correction cannot in general satisfy both Eqs. (6) and (7).

B. Minimal Methods

The discussion in the previous subsection makes it clear that that satisfying the two constraints Eq. (6) and Eq. (7) requires the use of at least two basis functions.

$$\bar{c}_N(\hat{x}) = c_N(\hat{x}) + a_1\phi_{N,1}(\hat{x}) + a_2\phi_{N,2}(\hat{x}) \tag{9}$$

We can then integrate the basis functions to develop constraints for the coefficients a_1 and a_2.

$$\Delta C_{N,1} = \int_{\hat{x}_1}^{\hat{x}_2} \phi_{N,1}(\hat{x})\,\mathrm{d}\hat{x} \qquad \Delta C_{m,1} = \int_{\hat{x}_1}^{\hat{x}_2} (\hat{x} - \hat{x}_{MRP})\phi_{N,1}(\hat{x})\,\mathrm{d}\hat{x} \tag{10}$$

$$\Delta C_{N,2} = \int_{\hat{x}_1}^{\hat{x}_2} \phi_{N,2}(\hat{x})\,\mathrm{d}\hat{x} \qquad \Delta C_{m,2} = \int_{\hat{x}_1}^{\hat{x}_2} (\hat{x} - \hat{x}_{MRP})\phi_{N,2}(\hat{x})\,\mathrm{d}\hat{x} \tag{11}$$

Then solving for the weights is simply a two-by-two system of linear equations.

$$\begin{bmatrix} \Delta C_{N,1} & \Delta C_{N,2} \\ \Delta C_{m,1} & \Delta C_{m,2} \end{bmatrix} \begin{bmatrix} a_1 \\ a_2 \end{bmatrix} = \begin{bmatrix} \bar{C}_N - C_N \\ \bar{C}_m - C_m \end{bmatrix} \tag{12}$$

This system will have a solution whenever the columns of the matrix are linearly independent.

The remaining question of this technique is how to select the adjustment functions $\phi_{N,1}$ and $\phi_{N,2}$. Selecting simple candidates such as the constant and linear offset from the previous section leads to difficulties because the candidate functions do not utilize any of the available information from the known sectional load profiles.

For example, there are often sections of the vehicle for which the local normal force is positive even when the angle of attack is negative; using a simple linear profile to adjust the sectional load profile will skew this. Adding a linear profile will also shift all the x-coordinates at which the normal force profile crosses zero. Adjustments to profiles near zero degrees angle of attack can also be problematic because small adjustments to C_N or C_m may require large local adjustments. Previous experience with a similar approach on Ares I-X [10] and SLS have demonstrated some of these pitfalls, and furthermore using only two adjustment functions may lead to a singular or poorly conditioned system of constraints.

C. Proper Orthogonal Decomposition

In order to make the shape of basis functions more directly related to the existing sectional loads, the use of a Proper Orthogonal Decomposition (POD) approach is considered. The POD approach is closely tied to the Singular Value Decomposition (SVD) approach. POD is a Reduced Order Model (ROM) technique that has been used for many aerospace applications [8, 11, 12]. It is a technique that identifies the primary signal from a large data set in a robust and automated way. This section describes how it can be applied to sectional load analysis using the sectional load profile from one CFD solution as the input "snapshot" and using a family of such solutions and snapshots to identify typical sectional load profiles.

For practical reasons, sectional loads on complex geometries are discretized into a number of slices using cuts at axial coordinates $x_1, x_2, \ldots, x_n$. The entire discretized sectional load profile at a single set of flight conditions (M_i, α_i, β_i) can be represented as a vector:

$$\mathbf{c}_{N,i} = \begin{bmatrix} c_{N,i,1} \\ c_{N,i,2} \\ \vdots \\ c_{N,i,n} \end{bmatrix} = \begin{bmatrix} c_N(x_1, M_i, \alpha_i, \beta_i) \\ c_N(x_2, M_i, \alpha_i, \beta_i) \\ \vdots \\ c_N(x_n, M_i, \alpha_i, \beta_i) \end{bmatrix} \tag{13}$$

where i is the case or flight condition index.

The sectional load vector $\mathbf{c}_{N,i}$ at one set of flight conditions is called a "snapshot." The POD technique works by collecting m snapshots into a single matrix:

$$\mathbf{C}_N = \begin{bmatrix} \mathbf{c}_{N,1} & \mathbf{c}_{N,2} & \cdots & \mathbf{c}_{N,n} \end{bmatrix} \tag{14}$$

We then compute a singular value decomposotion of the $n \times m$ matrix $\mathbf{C}_N$

$$\mathbf{C}_N = \mathbf{\Phi}_N \mathbf{\Sigma}_N \mathbf{V}_N^T \tag{15}$$

The matrix $\mathbf{\Phi}_N$ (note: this matrix is often written $\mathbf{U}$, but we are saving that letter of the alphabet for uncertainties, which will be discussed later) has column vectors that have the same dimension as the snapshot sectional load vectors.

$$\hat{\boldsymbol{\phi}}_{N,i} = \begin{bmatrix} \phi_{N,i,1} \\ \phi_{N,i,2} \\ \vdots \\ \phi_{N,i,n} \end{bmatrix} \tag{16}$$

The basis vectors also form an orthogonal matrix, so

$$\|\hat{\boldsymbol{\phi}}_{N,k}\|^2 = 1 \tag{17}$$

$$\hat{\boldsymbol{\phi}}_{N,j} \cdot \hat{\boldsymbol{\phi}}_{N,k} = \begin{cases} 1 & j = k \\ 0 & j \neq k \end{cases} \tag{18}$$

The matrix $\mathbf{\Sigma}_N$ is a rectangular matrix with so-called singular values along its diagonal.

$$\mathbf{\Sigma}_N = \begin{bmatrix} \sigma_{N,1} & 0 & \cdots & 0 \\ 0 & \sigma_{N,2} & & 0 \\ \vdots & & \ddots & \vdots \\ 0 & 0 & \cdots & \sigma_{N,m} \\ 0 & 0 & \cdots & 0 \\ \vdots & \vdots & & \vdots \\ 0 & 0 & \cdots & 0 \end{bmatrix} \tag{19}$$

Finally, the matrix $\mathbf{V}_N$ is defined so that the decomposition is correct. It provides the coefficients that allow one to reconstruct the original snapshots from the modes and singular values. While the technique discussed here does not use $\mathbf{V}_N$, alternative methods may use it to provide more information for optimal adjustments. The example above for $\mathbf{\Sigma}_N$ is for the case that $m > n$, but the extra block of zeros could be on the right if $m < n$. The singular values are positive real-valued numbers that describe how much energy is contained in or represented by the corresponding mode. By convention, these singular values are arranged in decreasing order, and they typically decrease in magnitude quickly. We can then select the first $K \leq m$ modes and use these as the candidates for adjusting the sectional load profile.

$$\bar{c}_N(\hat{x}) = c_N(\hat{x}) + \sum_{k=1}^{K} a_k \hat{\boldsymbol{\phi}}_{N,k}(\hat{x}) \tag{20}$$

Here K is the number of basis functions used as candidates for the adjustment, which must be at least as large as the number of constraints; and m is the number of snapshots and therefore the maximum number of basis functions the user may select.

Examples of these modes and how they compare to the original snapshots are demonstrated in Fig. 4. The original sectional load profiles calculated on the Block 1B crew configuration of SLS at Mach 1.30 and 33 combinations of α and β are shown in gray. Both the lateral force (CY) and normal force (CN) loads are

shown. The first mode to come out of the POD from these 33 snapshots is plotted in blue, and the second mode is plotted in green. Most noticeably, the first mode looks pretty much like a snapshot, and the second mode has more unique features. In addition, the legend of both plots in Fig. 4 indicates how much of the data can be described by each mode. In this example, over 60% of the data is contained in the first mode, and then the second through roughly sixth modes each contain a similar amount of descriptive capability.

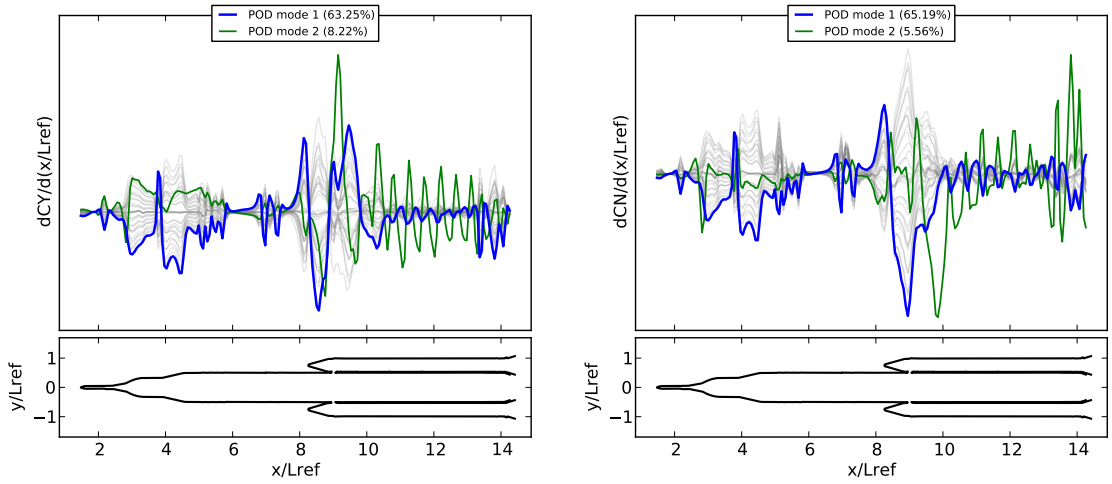

a)*CY* snapshots

b)*CN* snapshots

Figure 4. Snapshots (gray) and first and second modes from Mach 1.30 sectional loads on Block 1B Space Launch System configuration

Thus we have constructed an adjustment framework that is subject to only have two constraints, Eq. (6) and Eq. (7), and multiple degrees of freedom $a_1, \ldots, a_K$. In the next section a method is explored that further constrains the system and makes it possible to solve for the K weights.

D. Optimization

Next we must devise the method to choose weights $a_1, \ldots, a_K$ for the adjustment equation Eq. (20). The first step is to evaluate the increment to C_N and C_m caused by each of the candidate functions

$$\Delta C_{N,k} = \int_{\hat{x}_1}^{\hat{x}_2} \hat{\boldsymbol{\phi}}_{N,k}(\hat{x})\, \mathrm{d}\hat{x} \tag{21}$$

$$\Delta C_{m,k} = \int_{\hat{x}_1}^{\hat{x}_2} (\hat{x} - \hat{x}_{MRP}) \hat{\boldsymbol{\phi}}_{N,k}(\hat{x})\, \mathrm{d}\hat{x} \tag{22}$$

These can be combined into overall constraints on the integrated normal force and pitching moment

$$\bar{C}_N = C_N + \sum_{k=1}^{K} a_k \Delta C_{N,k} \tag{23}$$

$$\bar{C}_m = C_m + \sum_{k=1}^{K} a_k \Delta C_{m,k} \tag{24}$$

In order to provide $K-2$ more constraints, some form of optimization problem (or other decision metric) must be created. The primary indicator available is the singular values; therefore modes with higher singular

values should generally be preferred during the optimization process. This idea can even be put into common language by saying that the adjustment should look as much as possible like existing data.

Early experience showed that the second mode (with singular value $\sigma_{N,2}$) is somewhat problematic, and so it appears beneficial to bias against this second mode. To make this a more general rule not subject to the kind of human intervention that the previous sentence might suggest, the idea was developed to bias against modes with highly localized contributions. Including this concept in the objective function weights gives preference to relatively smooth adjustments.

The overall weight for each basis function's contribution to the objective function is

$$v_k = \max_{\hat{x}\in[\hat{x}_1,\hat{x}_2]} \hat{\boldsymbol{\phi}}_{N,k}(\hat{x}) \tag{25}$$

$$w_k = v_k/\sigma_{N,k} \tag{26}$$

Using these weights, we seek to minimize the L_2 norm of the total adjustment function.

$$\min_{\mathbf{w}\in\mathbb{R}^K} f(\mathbf{w}) = \sum_{k=1}^{K} w_k a_k^2 \tag{27}$$

In order to solve this minimization problem Eq. (27) subject to the constraints Eqs. (23) and (24), we can use Lagrange multipliers.

$$\begin{aligned} F(a_1,\ldots,a_K,\lambda_1,\lambda_2) = \lambda_1 &\left(\bar{C}_N - C_N - \sum_{k=1}^{K} a_k \Delta C_{N,k}\right) \\ &+ \lambda_2 \left(\bar{C}_{LM} - C_{LM} - \sum_{k=1}^{K} a_k \Delta C_{LM,k}\right) + \sum_{k=1}^{K} w_k a_k^2 \end{aligned}$$

To minimize this Lagrangian, we set the derivative of F with respect to each a_k and λ equal to zero.

$$\frac{\partial F}{\partial a_k} = -\lambda_1 \Delta C_{N,k} - \lambda_2 \Delta C_{LM,k} + 2 w_k a_k = 0 \tag{28}$$

This leads to a simple linear system of equations.

$$\begin{bmatrix} \Delta C_{N,1} & \Delta C_{N,2} & \cdots & \Delta C_{N,K} & 0 & 0 \\ \Delta C_{m,1} & \Delta C_{m,2} & \cdots & \Delta C_{m,K} & 0 & 0 \\ -2w_1 & 0 & \cdots & 0 & \Delta C_{N,1} & \Delta C_{m,1} \\ 0 & -2w_2 & \ddots & \vdots & \Delta C_{N,2} & \Delta C_{m,2} \\ \vdots & \ddots & \ddots & 0 & \vdots & \vdots \\ 0 & \cdots & 0 & -2w_K & \Delta C_{N,K} & \Delta C_{m,K} \end{bmatrix} \begin{bmatrix} a_1 \\ a_2 \\ \vdots \\ a_K \\ \lambda_1 \\ \lambda_2 \end{bmatrix} = \begin{bmatrix} \bar{C}_N - C_N \\ \bar{C}_m - C_m \\ 0 \\ 0 \\ \vdots \\ 0 \end{bmatrix} \tag{29}$$

The system of equations in Eq. (29) is readily solved by a typical linear algebra package. Furthermore, it is very resistant to stiffness as long as K is sufficiently smaller than m, the number of snapshots.

For the lateral loads, the process is almost identically repeated with C_Y and C_n in place of C_N and C_m, respectively. For the axial load, there is no corresponding moment adjustment. While adjusting C_A on its own is much less sensitive to mistakes, we use the same POD-based optimization with one less constraint.

$$\begin{bmatrix} \Delta C_{Y,1} & \Delta C_{Y,2} & \cdots & \Delta C_{Y,K} & 0 & 0 \\ \Delta C_{n,1} & \Delta C_{n,2} & \cdots & \Delta C_{n,K} & 0 & 0 \\ -2w_{Y,1} & 0 & \cdots & 0 & \Delta C_{Y,1} & \Delta C_{n,1} \\ 0 & -2w_{Y,2} & \ddots & \vdots & \Delta C_{Y,2} & \Delta C_{n,2} \\ \vdots & \ddots & \ddots & 0 & \vdots & \vdots \\ 0 & \cdots & 0 & -2w_{Y,K} & \Delta C_{Y,K} & \Delta C_{n,K} \end{bmatrix} \begin{bmatrix} a_{Y,1} \\ a_{Y,2} \\ \vdots \\ a_{Y,K} \\ \lambda_1 \\ \lambda_2 \end{bmatrix} = \begin{bmatrix} \bar{C}_Y - C_Y \\ \bar{C}_n - C_n \\ 0 \\ 0 \\ \vdots \\ 0 \end{bmatrix} \tag{30}$$

$$\begin{bmatrix} \Delta C_{A,1} & \Delta C_{A,2} & \cdots & \Delta C_{A,K} & 0 \\ -2w_{A,1} & 0 & \cdots & 0 & \Delta C_{A,1} \\ 0 & -2w_{A,2} & \ddots & \vdots & \Delta C_{A,2} \\ \vdots & \ddots & \ddots & 0 & \vdots \\ 0 & \cdots & 0 & -2w_{A,K} & \Delta C_{A,K} \end{bmatrix} \begin{bmatrix} a_{A,1} \\ a_{A,2} \\ \vdots \\ a_{A,K} \\ \lambda_1 \end{bmatrix} = \begin{bmatrix} \bar{C}_A - C_A \\ 0 \\ 0 \\ \vdots \\ 0 \end{bmatrix} \tag{31}$$

E. Implementation Details

Several additional procedural recommendations can be made based on experience using these adjustments with practical aerodynamic data. For a typical launch vehicle application, the ascent simulations cover a range of Mach numbers (e.g. Mach 0.5 to Mach 5.0) and a few different angles of attack and angles of sideslip at each Mach number.

Previous experience with launch vehicle line loads [13] has shown that different conditions (in particular, different values of α and β) at the same Mach number generally lead to similar sectional load profiles. Since the sectional load profiles are non-dimensional, this statement mostly refers to the shape of the profiles. The examples in Fig. 5, which both contain the normal force sectional load profile for nine different CFD solutions from FUN3D, demonstrate the similarities among cases of the same Mach number and differences with other Mach numbers.

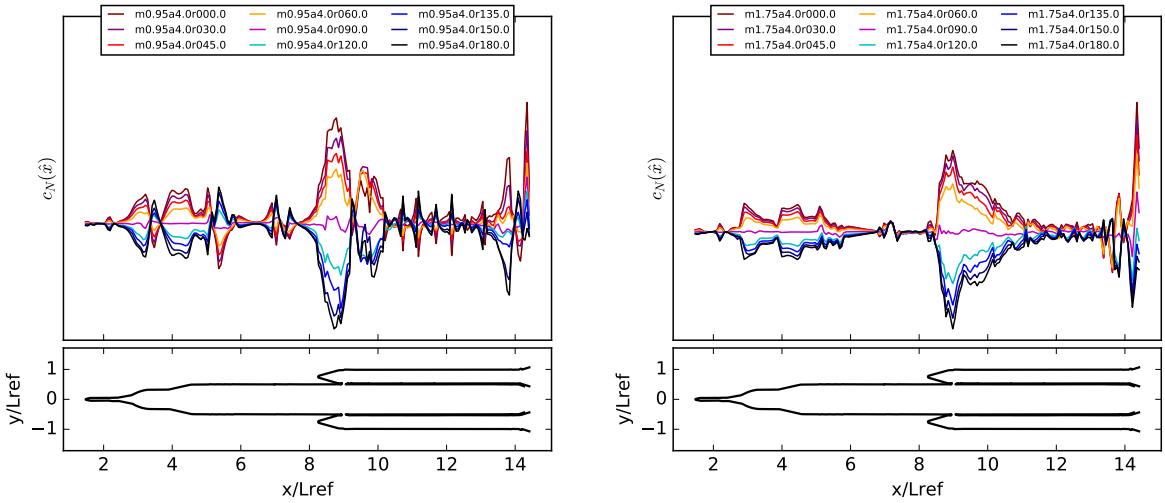

a)Mach 0.95 b)Mach 1.75

Figure 5. Sample *CN* sectional load profiles on the crewed Block 1B configuration at 4° total angle of attack, nonnegative sideslip, and two different Mach numbers

As a result of this observation, we take 33 or so sectional load profiles from the conditions inside the flight envelope at one Mach number as the snapshots for Eq. (14). Our CFD run matrix typically includes additional cases that are outside the flight envelope to support analysis of various abort scenarios. A consequence of this approach is that we need to recalculate the POD for each Mach number (for SLS, we use a run matrix of 19 different Mach numbers between 0.5 and 5.0 for ascent analysis).

Since Eq. (29) is linear, we can construct one adjustment function with ΔC_N=1 and ΔC_m=0 and another with ΔC_N=0 and ΔC_m=1. For Mach number M_j, we call these two adjustment profiles $\hat{\boldsymbol{\psi}}_{N,j}$ and $\hat{\boldsymbol{\psi}}_{m,j}$,

respectively.

$$\hat{\boldsymbol{\psi}}_{N,j}(\hat{x}) = \sum_{k=1}^{K} a_{N,k}\hat{\boldsymbol{\phi}}_{N,k}(\hat{x}) \tag{32}$$

$$\hat{\boldsymbol{\psi}}_{m,j}(\hat{x}) = \sum_{k=1}^{K} a_{m,k}\hat{\boldsymbol{\phi}}_{N,k}(\hat{x}) \tag{33}$$

These adjustments satisfy the following properties

$$\int_{\hat{x}_1}^{\hat{x}_2} \hat{\boldsymbol{\psi}}_{N,j}(\hat{x})\,\mathrm{d}\hat{x} = 1 \qquad \int_{\hat{x}_1}^{\hat{x}_2} (\hat{x} - \hat{x}_{MRP})\hat{\boldsymbol{\psi}}_{N,j}(\hat{x})\,\mathrm{d}\hat{x} = 0$$

$$\int_{\hat{x}_1}^{\hat{x}_2} \hat{\boldsymbol{\psi}}_{m,j}(\hat{x})\,\mathrm{d}\hat{x} = 0 \qquad \int_{\hat{x}_1}^{\hat{x}_2} (\hat{x} - \hat{x}_{MRP})\hat{\boldsymbol{\psi}}_{m,j}(\hat{x})\,\mathrm{d}\hat{x} = 1$$

Once these two basis functions have been calculated for a given Mach number, a generic adjustment can be constructed as a linear combination of them.

$$\bar{c}_N(\hat{x}) = c_N(\hat{x}) + \left(\bar{C}_N - C_N\right)\hat{\boldsymbol{\psi}}_{N,j}(\hat{x}) + \left(\bar{C}_m - C_m\right)\hat{\boldsymbol{\psi}}_{m,j}(\hat{x}) \tag{34}$$

As a result, the implementation only needs to calculate two adjustment functions for each Mach number (actually five: two for C_N, two more for C_Y, and one more for C_A). Although the calculation of these adjustment functions is quick (roughly a second using simple Python code on a current workstation), trajectory and structural analysis may need to query the database at thousands of different flight conditions. As a result, eliminating the roughly one-second calculation still provides significant savings depending on the application.

F. Uncertainty Quantification

A typical force and moment database for a modern aerospace vehicle will include an uncertainty distribution on each of the six integrated force & moment coefficients. This uncertain force and moment database can then be incorporated into a Monte Carlo distribution in which all of the possible values are considered in some larger simulation (such as an ascent trajectory simulation). This typically takes the following form where U_{CN} is the uncertainty in CN (and therefore a single fixed value for a given flight condition) and ε_{CN} is a random variable sampled from the appropriate probability distribution function.

$$\tilde{C}_A = C_A + \varepsilon_{CA}U_{CA} \tag{35}$$

$$\tilde{C}_N = C_N + \varepsilon_{CN}U_{CN} \tag{36}$$

$$\tilde{C}_m = C_m + \varepsilon_{CLM}U_{CLM} + \varepsilon_{CN}U_{CN}\frac{x_{MRP} - x_{cg}}{L_{ref}} \tag{37}$$

$$\tilde{C}_Y = C_Y + \varepsilon_{CY}U_{CY} \tag{38}$$

$$\tilde{C}_n = C_n + \varepsilon_{CLN}U_{CLN} + \varepsilon_{CY}U_{CY}\frac{x_{MRP} - x_{cg}}{L_{ref}} \tag{39}$$

The dispersion function for the pitching moment (C_m) has an extra term because the integrated pitching moment is inherently correlated with dispersions of the normal force. This form of the equation assumes that the normal force is uncorrelated with the pitching moment about the center of gravity, although in some applications x_{cg} is replaced with the coordinate of the "balance moment center," i.e. the location about which wind tunnel moments were measured.

Then a simple uncertainty quantification methodology for a sectional loads database is to pick many values of ε_{CN}, ε_{CLM}, etc. and then apply Eqs. (29), (30), and (31) for each dispersed integrated force and moment value.

To implement this uncertainty dispersion, the reference functions described in Sec. II.E are particularly convenient. For example, for a flight condition with Mach number M_j, a dispersed sectional load profile $\tilde{c}_N(\hat{x})$ can be determined using the random draws ε_{CN} and ε_{CLM}.

$$\begin{aligned}\tilde{c}_N(\hat{x}) = \bar{c}_N(\hat{x}) &+ \varepsilon_{CN} U_{CN} \hat{\boldsymbol{\psi}}_{N,j}(\hat{x}) \\ &+ \left(\varepsilon_{CLM} U_{CLM} + (\hat{x}_{MRP} - \hat{x}_{cg}) \varepsilon_{CN} U_{CN}\right) \hat{\boldsymbol{\psi}}_{m,j}(\hat{x})\end{aligned} \tag{40}$$

G. Additional UQ Uncorrelated to Forces & Moments

In addition to this contribution to disperse the line load profiles in a manner consistent with the force & moment database, there is a method to disperse the line loads in a random fashion. The motivation for this technique is to cover additional variations in how a load might be distributed. Otherwise there is exactly one line load for every fixed set of flight conditions and integrated forces and moments. We cannot really expect this level of determinism from a CFD solution, and furthermore a deterministic line load does not account for possible minor changes to the geometry.

To enable this further dispersion without putting too much burden on a user of the dispersed database, we seek a third perturbation mode to the *CN* profile that changes neither the integrated normal force nor the pitching moment. To find such a mode using a mode recommended by the POD, we modify the Lagrangian used in Sec. D with a third constraint

$$\begin{aligned}F(a_1, \ldots, a_K, \lambda_1, \lambda_2, \lambda_3) = &- \lambda_1 \sum_{k=1}^{K} a_k \Delta C_{N,k} \\ &- \lambda_2 \sum_{k=1}^{K} a_k \Delta C_{m,k} + \lambda_3 \left(1 - \sum_{k=1}^{K} a_k\right) + \sum_{k=1}^{K} w_k a_k^2\end{aligned}$$

It would be ideal to replace the λ_3 term with a quadratic norm instead of the sum used here. However, the Lagrangian problem could no longer be solved as a linear system. Using an L_1 norm like this appears to permit solutions with large but oscillating (some positive, some negative) values of a_k, but the objective function term at the end suppresses large magnitudes of a_k and keeps the system stable.

This leads to a slightly modified linear system of equations with one more row and one more column than the previous version.

$$\begin{bmatrix} \Delta C_{N,1} & \Delta C_{N,2} & \cdots & \Delta C_{N,K} & 0 & 0 & 0 \\ \Delta C_{m,1} & \Delta C_{m,2} & \cdots & \Delta C_{m,K} & 0 & 0 & 0 \\ 1 & 1 & \cdots & 1 & 0 & 0 & 0 \\ -2w_1 & 0 & \cdots & 0 & \Delta C_{N,1} & \Delta C_{m,1} & 1 \\ 0 & -2w_2 & \ddots & \vdots & \Delta C_{N,2} & \Delta C_{m,2} & 1 \\ \vdots & \ddots & \ddots & 0 & \vdots & \vdots & 1 \\ 0 & \cdots & 0 & -2w_K & \Delta C_{N,K} & \Delta C_{m,K} & 1 \end{bmatrix} \begin{bmatrix} a_1 \\ a_2 \\ \vdots \\ a_K \\ \lambda_1 \\ \lambda_2 \\ \lambda_3 \end{bmatrix} = \begin{bmatrix} 0 \\ 0 \\ 1 \\ 0 \\ 0 \\ \vdots \\ 0 \end{bmatrix} \tag{41}$$

It is possible to construct further dispersion modes that do not affect *CN* and *CLM* that are different from this solution. To do this, repeat the process again but with an additional constraint that the second mode is perpendicular to the first mode. Suppose that we use b for the weights of this second mode instead of a, then

we can construct the following:

$$F(b_1,\ldots,b_K,\lambda_1,\ldots,\lambda_4) = -\lambda_1 \sum_{k=1}^{K} b_k \Delta C_{N,k} - \lambda_2 \sum_{k=1}^{K} b_k \Delta C_{m,k} + \lambda_3 \left(1 - \sum_{k=1}^{K} b_k\right) + \lambda_4 \sum_{k=1}^{K} a_k b_k + \sum_{k=1}^{K} w_k b_k^2$$

These are just examples of extending the method using different additional constraints, and are potential avenues for forward research. In the following section, results of the adjustment process given by Eqs. (29), (30), and (31) are presented.

III. Adjustment Results

Some examples comparing the original sectional loads extracted directly from the raw CFD solutions to the adjusted results can be found in Figs. 6 and 7. The original loads are shown in black, and the adjusted loads are shown in red. Although the adjusted loads could be considered the primary data, this format seems to highlight the differences more strongly than other plotting formats that were tried.

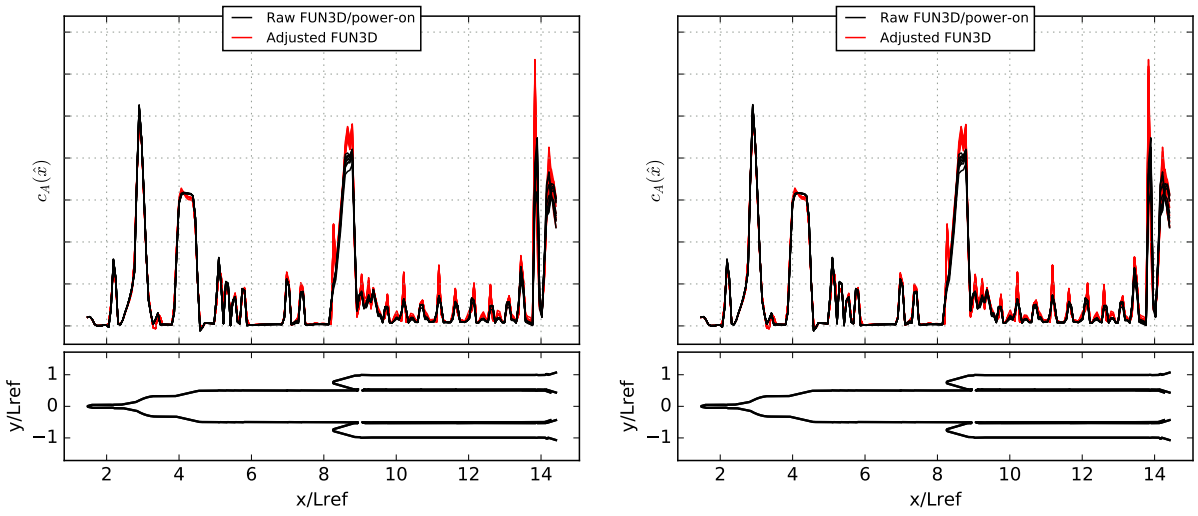

a) $C_A, \beta \leq 0$ b) $C_A, \beta \geq 0$

Figure 6. Original sectional axial loads from CFD (black) and loads adjusted to match wind-tunnel forces and moments (red) for Mach 1.3 flight conditions of SLS Block 1B with 4° total angle of attack

Figures 6 and 7 are shown for Mach 1.3, which was the Mach number for which the largest adjustments were made. Naturally, this means that these are the easiest cases to visualize the differences between the nominal and adjusted load profiles. Furthermore, the figures highlight flight conditions at 4° total angle of attack and a variety of roll angles. This 4° choice corresponds to the official flight envelope for the vehicle (at this Mach number). Although the vehicle is expected to fly at much lower total angles of attack, these edge cases drive the structural design of the vehicle.

In Fig. 6 and 7, the conditions with negative sideslip are shown on the left, and the conditions with positive sideslip are shown on the right. To be precise, the cases with precisely zero sideslip are shown in both figures. There are 9 black curves and 9 red curves in each figure even though there are only 16 total curves.

In Fig. 6, adjustments to *CA* are plotted for all 16 of these Mach 1.3 conditions. These loads are very similar for each vehicle roll angle, so the different black and red lines in Fig. 6 are mostly on top of each

other. The local $c_A(\hat{x})$ adjustments are roughly the same as multiplying the entire load profile by the required factor to match the higher wind tunnel *CA* measurement. However, there are a few differences. First, the adjustments to the forward portion of the vehicle (up to x/L_{ref}=4) are very small. This indicates that all of the snapshots used to create the POD basis had almost the same profile on that portion, and so it is considered a weak candidate for adjustment. There is also a feature in the adjusted loads (red curves) just after x/L_{ref}=4, which is created by the bow shock from the noses of the two Solid Rocket Boosters interact with a flange on the core body.

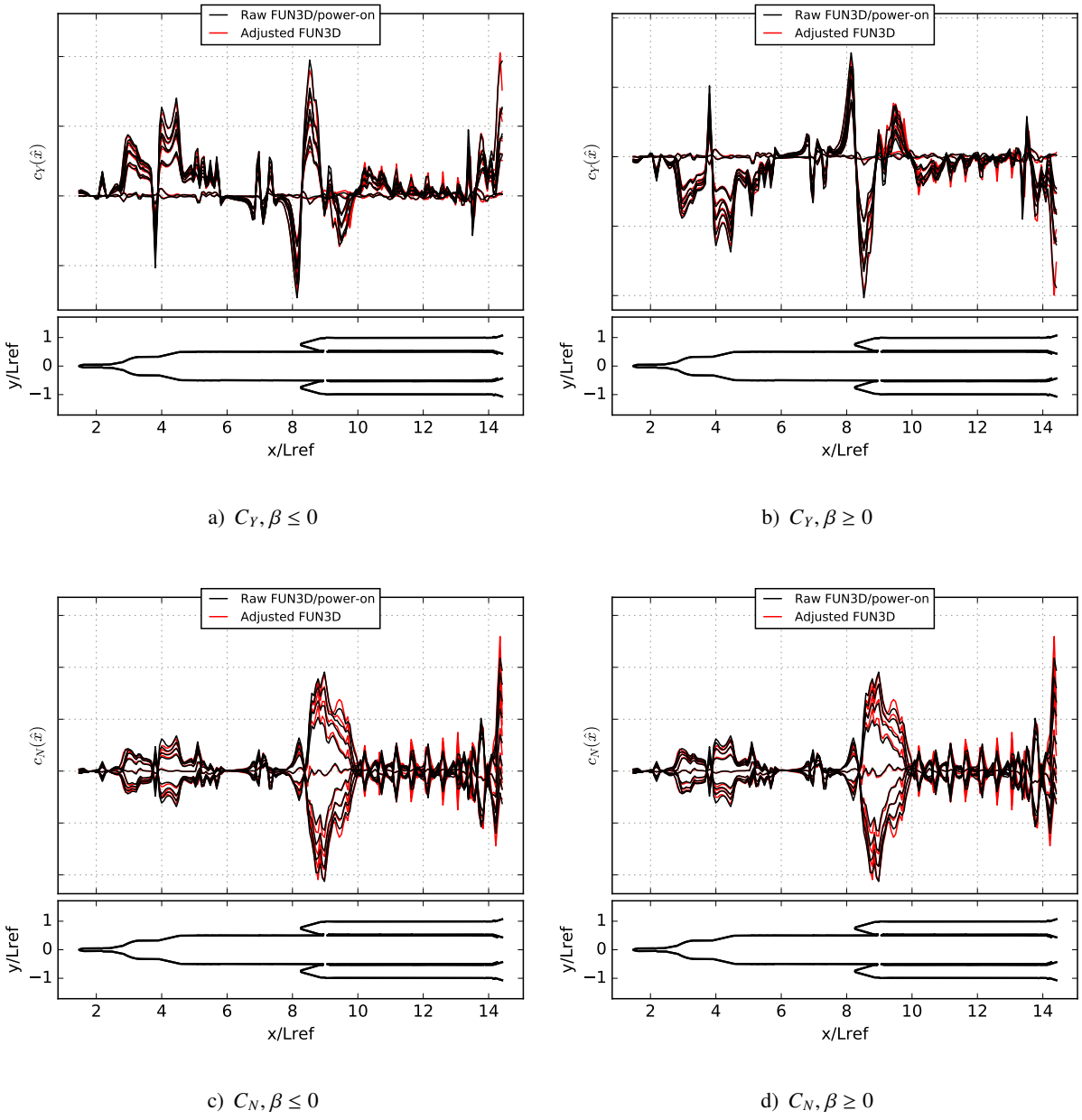

a) $C_Y, \beta \leq 0$

b) $C_Y, \beta \geq 0$

c) $C_N, \beta \leq 0$

d) $C_N, \beta \geq 0$

Figure 7. Original sectional lateral and normal loads from CFD (black) and loads adjusted to match wind-tunnel forces and moments (red) for all Mach 1.3 flight conditions with 4° total angle of attack

The plots of *CY* adjustments in Figs. 7a and 7b show that there are very small adjustments to the side force, and the adjustments to the line load profiles are correspondingly small. Unlike the *CA* and *CN* plots, the left and right plots are roughly mirrors. This is because side force is roughly proportional to β, and we

have filtered the two plots using β.

Adjustments to *CN* for Mach 1.3, shown in Fig. 7c and 7d, show medium-sized adjustments. This situation in which differences between CFD and wind tunnel (and also between two different CFD solvers or between two different wind tunnel tests) is larger for *CN* than *CY* for SLS. This is likely due to the added complexity of air flowing between the main core body and the solid rocket boosters. This complication has less of an effect on *CY*, and so the results are more consistent.

The location of $\hat{x}_{MRP}$ in this work is at the base of the core vehicle, but this does not affect the results of the adjustment as long as the value of the integrated pitching moment coefficient C_m is shifted in accordance with the moment reference point. Recall that the normal force sectional load profile, $c_N(\hat{x})$ affects the integrated pitching moment coefficient, so separate plots for the pitching moment profile are not necessary.

Differences between the black and red curves in Fig. 7 are largest around the forward attach hardware between x/L_{ref} values of 8 and 10 with additional small spikes of differences over the portion of the vehicle aft of this point. This forward attach hardware is known from experimentation and higher-fidelity CFD solutions to be a highly complex and unsteady region of the flow, so it appears to be a good result that some of the larger adjustments are located there. Conversely, the forward portion of the vehicle has fewer wakes and other sources of unsteadiness, and so the smaller adjustments there are consistent with the higher confidence in the corresponding sections of the load profile.

Another noteworthy factor in Figs. 7c and 7d is the small adjustments to the curve in the center of each plot. These are for cases with perfect sideslip, i.e. α=0°. It may seem like a small accomplishment to adjust this small *CN* profile, but adjusting this profile to match a target integrated normal force and pitching moment simultaneously can have problems when using overly simple methods. In particular, problems often arise because a small adjustment to either integrated load may require a sign change, which has obvious implications if the user attempts to simply scale the load profile (as explained in Sections II.A and II.B).

To provide another example of adjustments, and to demonstrate how sectional loads from different Mach numbers are qualitatively different, Fig. 8 shows the original CFD and adjusted C_Y and C_N sectional loads for Mach 3.0. The results are for 6° total angle of attack because the SLS flight envelope expands from 4° to 6° at Mach 2.5. The difference between black and red lines are smaller in these results, reflecting a closer agreement between CFD and wind tunnel results at these conditions.

In addition, the Mach 3.0 profiles all look quite similar to each other (after applying a scale factor) but quite different from the Mach 1.3 results. This is relevant because developers must make a decision about which snapshots are included in the POD. The combination of Figs. 7 and 8 demonstrate why snapshots are grouped by Mach number for this database, but in general users can try multiple groupings and use the singular values to decide which grouping is most appropriate. A POD with higher first and second singular values is usually an indication of a better grouping, although making general statements for this class of engineering problem is not always possible.

IV. Uncertainty Quantification Results

This section demonstrates a small number of examples of dispersed sectional load profiles. Two flight conditions, both around maximum dynamic pressure for the SLS Block 1B vehicle, are highlighted: one at 4° angle of attack with 0° sideslip and one at 4° sideslip angle with 0° angle of attack.

The first example in Fig. 9 shows the distribution of the $\tilde{c}_N(\hat{x})$ profile (sectional normal force coefficient) for the zero-sideslip case. In Fig. 9a, only the integrated normal force is dispersed, and the pitching moment about the center of gravity is kept constant. The thick black curve is the adjusted $\bar{c}_N(\hat{x})$ profile as discussed in the previous section; that is, it is adjusted to match the *CN* measured in the wind tunnel. Then a selection of values for ε_{CN} are made (from Eq. (36)). In Fig. 9, positive values of ε_{CN} have red curves, while negative values of ε_{CN} have blue curves.

In Fig. 9a, the dispersed set of sectional loads are simply the base load (black curve) plus ε_{CN} times a common adjustment load. Therefore the load at any x-coordinate varies linearly with ε_{CN}. However, there are locations at which the blue curves are above the nominal profile. At these locations, the local $c_N(\hat{x})$ must change in the opposite direction as integrated *CN* in order to preserve the pitching moment.

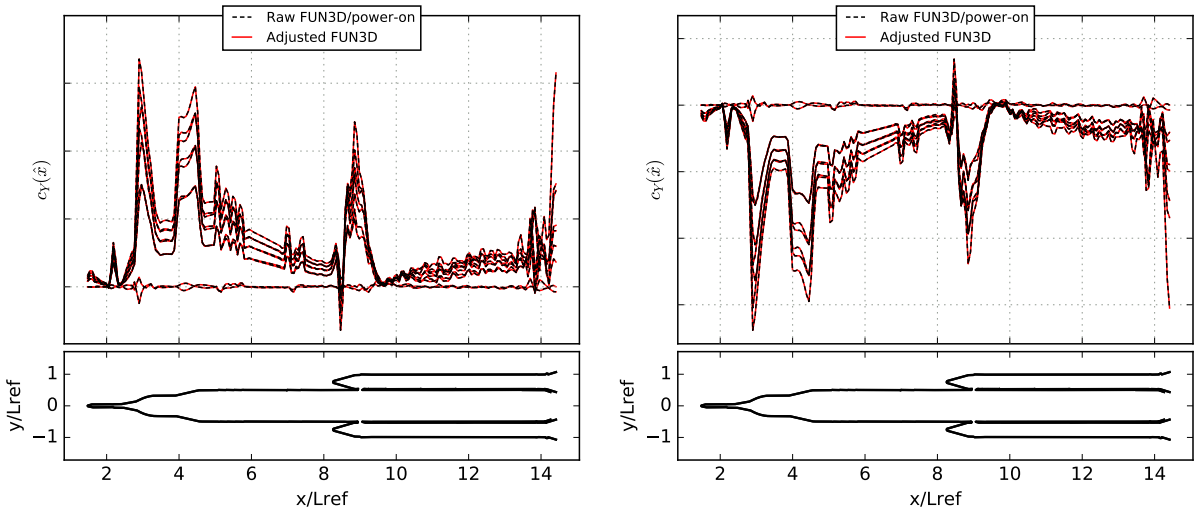

a) $C_Y, \beta \leq 0$

b) $C_Y, \beta \geq 0$

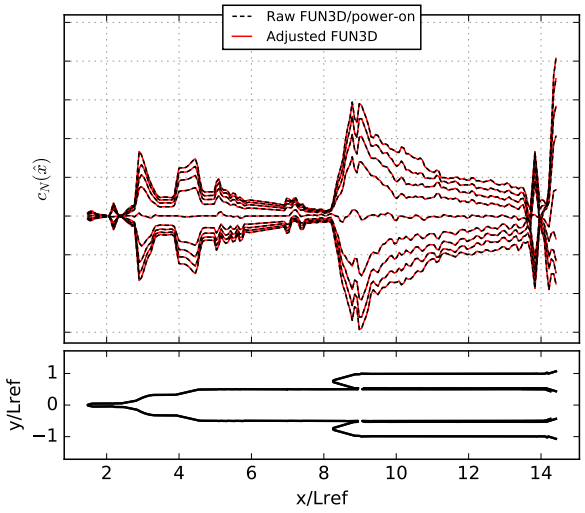

c) $C_N, \beta \leq 0$

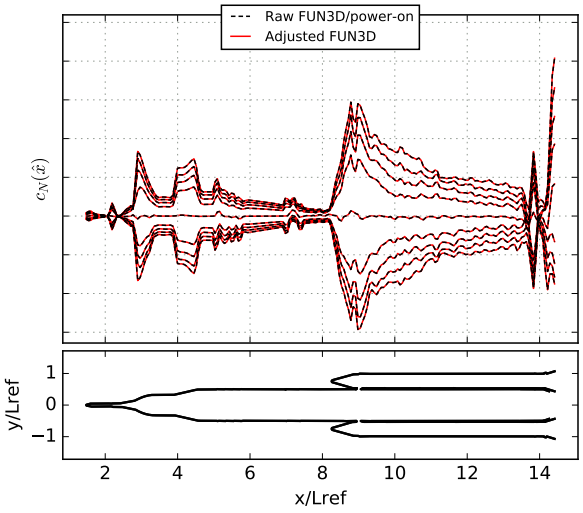

d) $C_N, \beta \geq 0$

Figure 8. Original sectional lateral and normal loads from CFD (black) and loads adjusted to match wind-tunnel forces and moments (red) for Mach 3.0 flight conditions of SLS Block 1B with 6° total angle of attack

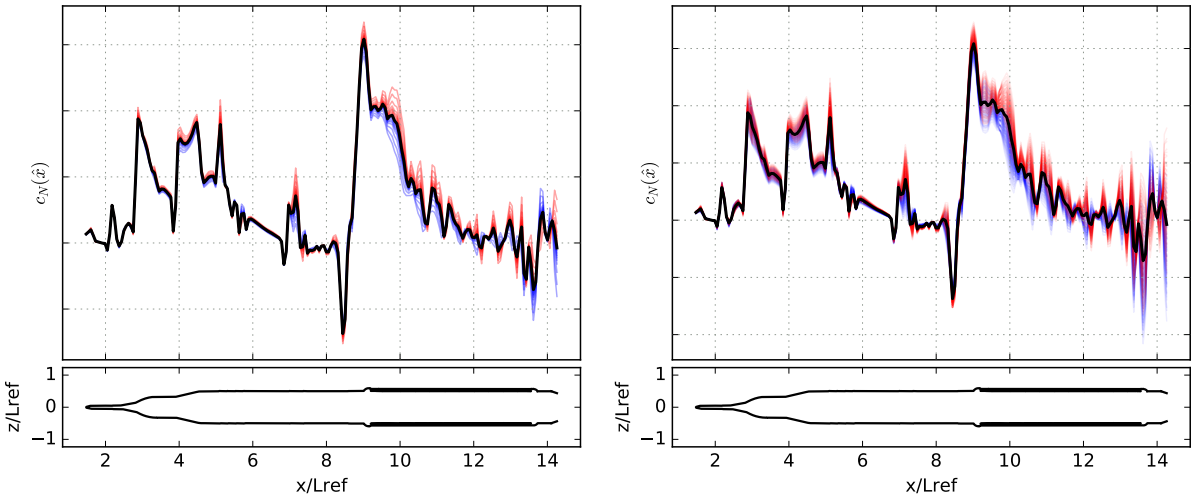

a) Dispersed C_N with ε_{CLM}=0

b) Dispersed C_N with $\varepsilon_{CLM}\neq$0

Figure 9. Dispersed sectional *CN* for SLS Block 1B at Mach 1.75, α=4°, β=0°. Red curves are for increases to integrated *CN*, and blue curves are for decreases in *CN*.

Figure 9b simultaneously disperses both integrated normal force (*CN*) and pitching moment (*CLM*). The normal force and pitching moment about the center of gravity are dispersed independently. There are more curves because dispersions of both integrated loads are considered, but the choice of colors is the same as 9a. Some regions of the plot are purple, which means that the local $\tilde{c}_N(\hat{x})$ can change in either direction depending on the value of ε_{CLM}.

The results of Fig. 9b are shown in two more formats in Fig. 10. Figure 10a is very similar to the previous figure except that the solid lines showing the adjusted loads are replaced with filled patches. In particular, the region between the primary (black) curve and each dispersed load is filled in with either a blue or red area. Each load uses a mostly transparent patch, so that it is possible to see some effect of the patches that are behind. Meanwhile, Fig. 10b shows the same set of curves but with red now representing an increase in the pitching moment (about the center of gravity) and blue a decrease. The fact that Fig. 10b has less purple pixels suggests that local shifts to the $\tilde{c}_N(\hat{x})$ profile are better correlated to ε_{CLM} than ε_{CN}.

For the same flight conditions as the previous figures, Fig. 11 shows the dispersions in the side force (*CY*) sectional loads. Because the sideslip angle is zero for this case, the baseline *CY* load is very small, and the dispersions look large compared to the amplitude of the black curve. The left figure, Fig. 11a, colors the dispersions by changes to the integrated force while the right figure, Fig. 11b, colors the same dispersions by the sign of the change to the yawing moment. Since Fig. 11b has more purple, the $\tilde{c}_Y(\hat{x})$ dispersions are better correlated to changes in integrated *CY* than integrated *CLN*.

In order to provide an example of a $\tilde{c}_Y(\hat{x})$ dispersion in which the baseline is not so small, Fig. 12 shows the dispersions for flight conditions at Mach 1.75 with zero angle of attack and 4° sideslip. In these figures, the dispersions are small relative to the magnitude of the baseline load (black curve), and as in Fig. 11 the local shifts to the sectional load profile correlate better with ε_{CY} than ε_{CLN}.

These figures (9–12) are good visualizations of the dispersed line load, but users of this type of data may require additional information or processing. A very common application of an aerodynamic sectional load database is to calculate an overall bending moment from each sectional load profile. For such an application, the user of the database should calculate the bending moment for several dispersed values of ε_{CN}, etc. The result is a histogram or probability density function of the bending moment for each condition. Such a process is additional work for the user of the data, but it is also rewarding because it allows the user to

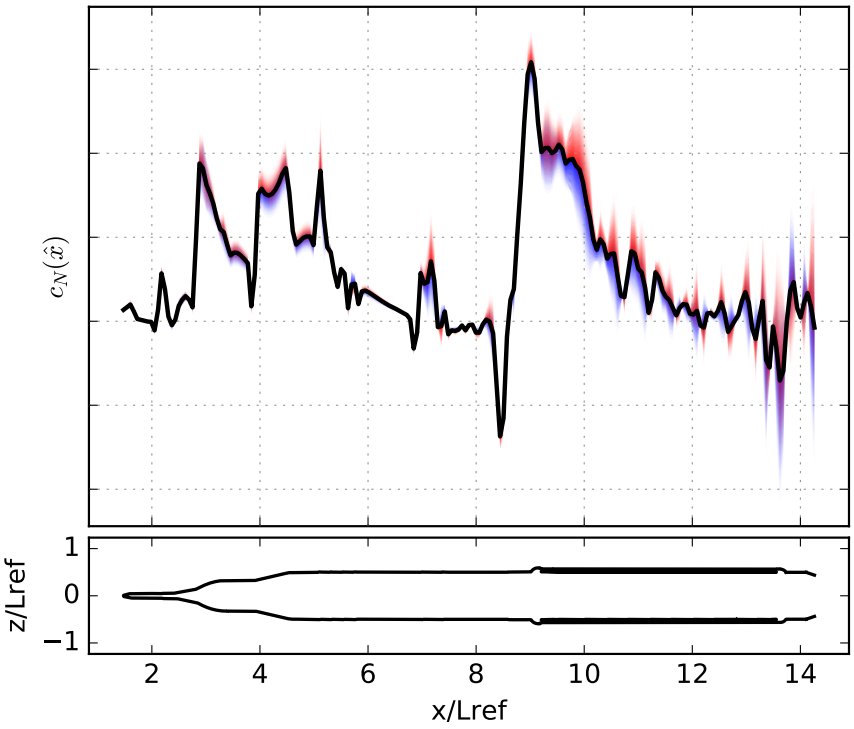

a) Dispersed C_N colored by ε_{CN}

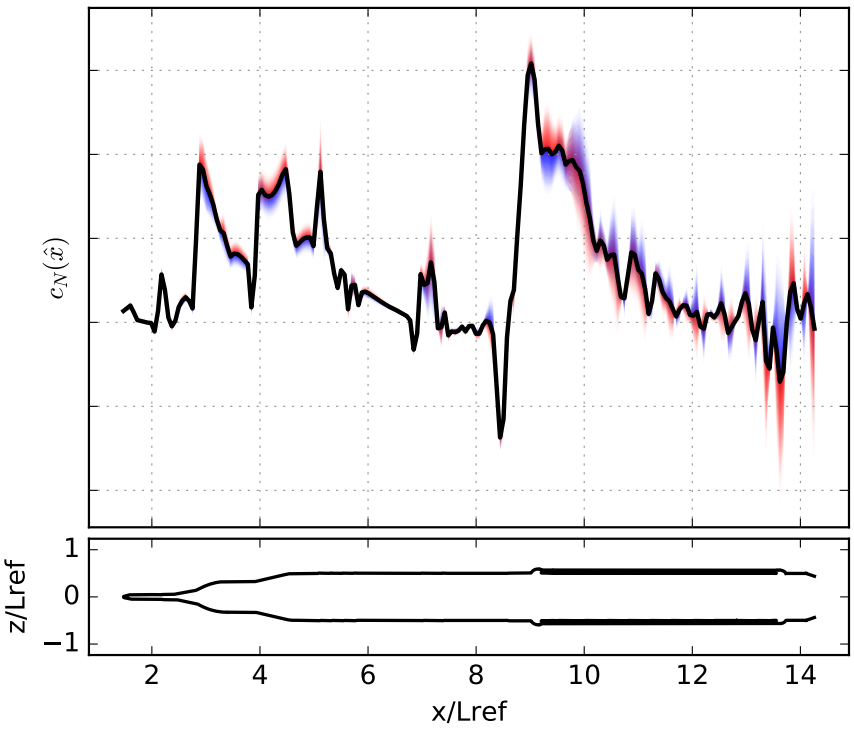

b) Dispersed C_N colored by ε_{CLM}

Figure 10. Dispersed sectional *CN* on the core body of SLS Block 1B at Mach 1.75, $\alpha = 4°$**,** $\beta = 0°$

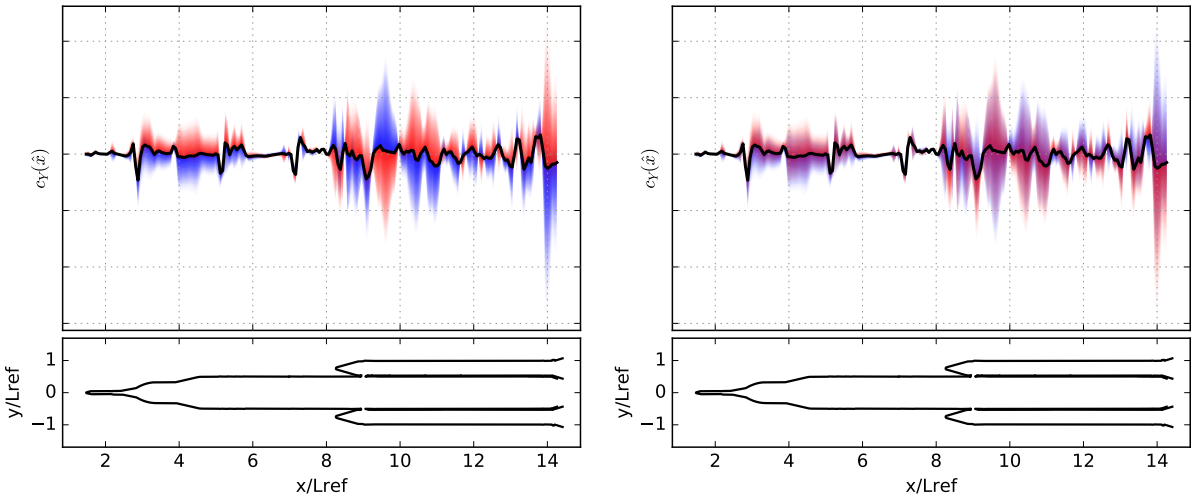

a) Dispersed C_Y colored by ε_{CY}

b) Dispersed C_Y colored by ε_{CLN}

Figure 11. Dispersed sectional *CY* on the core body of SLS Block 1B at Mach 1.75, $\alpha = 4°, \beta = 0°$

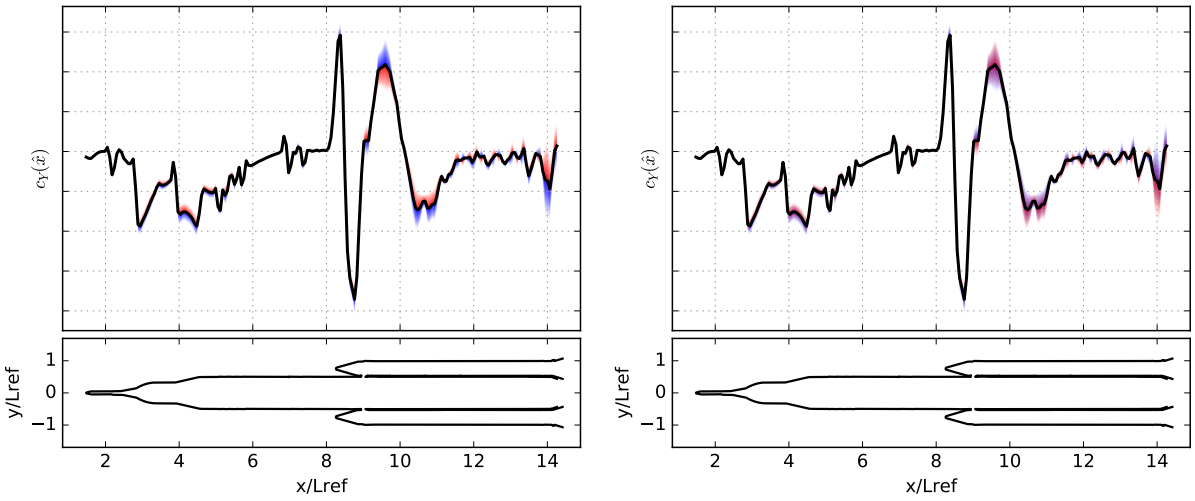

a) Dispersed C_Y colored by ε_{CY}

b) Dispersed C_Y colored by ε_{CLN}

Figure 12. Dispersed sectional *CY* on the core body of SLS Block 1B at Mach 1.75, $\alpha = 0°, \beta = 4°$

translate the aerodynamic uncertainty quantification into information about the uncertainty in the bending moment.

Similarly, another application of an aerodynamic sectional load database is to use it as the basis for a flight simulation including aeroelastic bending. In this case, the user is probably already performing a Monte Carlo analysis in which many inputs to the simulation are varied randomly, and this tells such a user how to fully account for uncertainty in the integrated forces and moments.

This uncertainty quantification method focuses on databases that describe changes in flight conditions. It can easily be extended to support geometry changes, provided a reasonable set of snapshots for different geometries can be parametrized and calculated. The approach is also different from Barth's [14] approach to *a posteriori* uncertainty quantification, which uses an ensemble of CFD solutions to estimate sensitivity to uncertainty in parameters such as the freestream Mach number.

In general, the approach in this paper inherits the magnitude of its uncertainty dispersions from the uncertainty in the wind tunnel force & moment database, and CFD sources of uncertainty are not directly discussed. In practice, the force & moment database may include a term from uncertainty in the CFD solutions, especially if a CFD increment added to the wind tunnel measurements. Adding to the dispersions to support additional sources of uncertainty is possible using the methods discussed in Sec. II.G. The list of CFD solutions in the database could also help to enable additional uncertainty quantification or improve the accuracy of this procedure. For example, if users are concerned that the sectional loads are sensitive to the choice of turbulence model, a subset of the solutions could be repeated using an alternative model, and then the multiple solutions at identical flight conditions can be added as snapshots to the POD.

V. Extensions and Alternatives

Some elements of this sectional load dispersion technique have relevance to any situation in which a multi-dimensional database must be adjusted or dispersed while maintaining consistency with scalar constraints. In the examples discussed in the preceding discussion, the dimension of the database entries being adjusted or dispersed was one. That is, adjustments were being made to one-dimensional data sets. Each adjustment was subject to one (*CA*) or two (*CY* and *CN*) constraints.

The algorithms are not substantially complicated by increasing the dimension of the dispersed data. One example is to consider surface pressure solutions as the snapshots to the POD instead of sectional load profiles. In the methods discussed in previous sections, *CY* and *CN* have separate adjustments, which are applied independently and are not necessarily consistent with with any particular surface pressure. An alternative approach that is more self-consistent is to derive the the line load adjustments directly from surface pressure snapshots. Let $\mathbf{p}_i$ be the surface pressure solution from case i run at flight conditions of M_i, α_i and β_i. The vector of discretized surface pressure coefficients from the CFD solution is an appropriate construction for $\mathbf{p}_i$, but optionally resampling the surface to develop smaller snapshots is also possible. These snapshots (again from a fixed Mach number if following the methods described previously in this paper) are assembled into a quite large data matrix

$$\mathbf{P} = \begin{bmatrix} \mathbf{p}_1 & \mathbf{p}_2 & \cdots & \mathbf{p}_m \end{bmatrix}$$

The POD of this matrix leads to basis modes $\hat{\boldsymbol{\phi}}_1, \hat{\boldsymbol{\phi}}_2, \ldots, \hat{\boldsymbol{\phi}}_K$ that now represent a change in surface pressure at every point on the surface of the vehicle. The modes have singular values $\sigma_1, \sigma_2, \ldots, \sigma_K$, respectively.

Furthermore, it is possible to integrate these surface pressures to calculate $\Delta C_{A,k}$, $\Delta C_{Y,k}$, $\Delta C_{N,k}$, $\Delta C_{\ell,k}$, $\Delta C_{m,k}$, and $\Delta C_{n,k}$ for each mode $\hat{\boldsymbol{\phi}}_k$. This leads to a simple extension of Eq. (29) to simultaneously adjust all

six force & moment coefficients.

$$\begin{bmatrix} \Delta C_{A,1} & \Delta C_{A,2} & \cdots & \Delta C_{A,K} & 0 & \cdots & 0 \\ \Delta C_{Y,1} & \Delta C_{Y,2} & \cdots & \Delta C_{Y,K} & 0 & \cdots & 0 \\ \Delta C_{N,1} & \Delta C_{N,2} & \cdots & \Delta C_{N,K} & 0 & \cdots & 0 \\ \Delta C_{\ell,1} & \Delta C_{\ell,2} & \cdots & \Delta C_{\ell,K} & 0 & \cdots & 0 \\ \Delta C_{m,1} & \Delta C_{m,2} & \cdots & \Delta C_{m,K} & 0 & \cdots & 0 \\ \Delta C_{n,1} & \Delta C_{n,2} & \cdots & \Delta C_{n,K} & 0 & \cdots & 0 \\ -2w_1 & 0 & \cdots & 0 & \Delta C_{A,1} & \cdots & \Delta C_{n,1} \\ 0 & -2w_2 & \ddots & \vdots & \Delta C_{A,2} & \cdots & \Delta C_{n,2} \\ \vdots & \ddots & \ddots & 0 & \vdots & & \vdots \\ 0 & \cdots & 0 & -2w_K & \Delta C_{A,K} & \cdots & \Delta C_{n,K} \end{bmatrix} \begin{bmatrix} a_1 \\ a_2 \\ \vdots \\ a_K \\ \lambda_1 \\ \lambda_2 \\ \lambda_3 \\ \lambda_4 \\ \lambda_5 \\ \lambda_6 \end{bmatrix} = \begin{bmatrix} \bar{C}_A - C_A \\ \bar{C}_Y - C_Y \\ \bar{C}_N - C_N \\ \bar{C}_\ell - C_\ell \\ \bar{C}_m - C_m \\ \bar{C}_n - C_n \\ 0 \\ 0 \\ \vdots \\ 0 \end{bmatrix} \tag{42}$$

Solving this system six times (one for an increment in CA, another for an increment in CY, and so on) results in a set of surface pressure deltas that can be used to construct an estimate of the surface pressure for any wind-tunnel–based or uncertainty-derived adjustments to the integrated forces and moments. Each of these six modes has the same data structure of a surface pressure, and it is possible to calculate a line load using it.

For example let $\hat{\boldsymbol{\phi}}_{A,j}$ be the surface pressure profile at Mach number M_j that adjusts C_A by 1.0 and leaves the other forces & moments unchanged. This is a triangulated surface (or whatever the structure of the surface grid may be) of pressures, so we can calculate sectional load profiles using this surface. Let the three profiles be $\hat{\boldsymbol{\psi}}_{A,A,j}$, $\hat{\boldsymbol{\psi}}_{A,Y,j}$, and $\hat{\boldsymbol{\psi}}_{A,N,j}$. Note that there are three of these sectional load profiles; even though we specify that there is no change to integrated C_Y, there may be local changes that result in a nontrivial sectional load profile. Then the dispersed sectional loads are

$$\begin{aligned} \bar{c}_N(\hat{x}) = c_N(\hat{x}) &+ \left(\bar{C}_A - C_A\right)\hat{\boldsymbol{\psi}}_{A,N}(\hat{x}) + \left(\bar{C}_Y - C_Y\right)\hat{\boldsymbol{\psi}}_{Y,N}(\hat{x}) + \left(\bar{C}_N - C_N\right)\hat{\boldsymbol{\psi}}_{N,N}(\hat{x}) \\ &+ \left(\bar{C}_\ell - C_\ell\right)\hat{\boldsymbol{\psi}}_{\ell,N}(\hat{x}) + \left(\bar{C}_m - C_m\right)\hat{\boldsymbol{\psi}}_{m,N}(\hat{x}) + \left(\bar{C}_n - C_n\right)\hat{\boldsymbol{\psi}}_{n,N}(\hat{x}) \end{aligned} \tag{43}$$

$$\bar{c}_\eta(\hat{x}) = c_\eta(\hat{x}) + \sum_{\nu \in [A,Y,N,\ell,m,n]} \left(\bar{C}_\nu - C_\nu\right)\hat{\boldsymbol{\psi}}_{\nu,\eta}(\hat{x}) \qquad \text{for } \eta \in [A, Y, \ell, m, n] \tag{44}$$

Technically, including viscous forces in these adjustments would be a better solution than just using the surface pressures. Several ways to integrate these forces exist. One is to simply include the directional skin friction coefficients in all three directions in the snapshots. This makes the snapshots four times larger, but the rest of the process remains the same. An alternative would be to calculate the three components of the local forces from both pressure and viscous forces, but this creates a change to the line load calculation procedure (although not a complex change).

Creating the POD for surface pressure solutions greatly increases the size of each snapshot, and in initial trials this means each POD takes several minutes on a current workstation. Memory may be a more critical limitation when working with large snapshots, and to avoid issues with memory, it may be appropriate to down-sample the surface to a coarser grid. Quite often the required mesh size to calculate an accurate CFD solution is much larger than what is required by the customers of a surface pressure database.

This discussion, which extends the adjustment/dispersion methodology to surface pressures, demonstrates the ease with which it can be applied to different problems. Adding more constraints to the problem simply involves adding more rows and columns to a system of equations such as that in Eq. (42). For example, forcing the adjusted/dispersed surface pressure to match a C_p value measured by a specific pressure tap in a wind tunnel or flight test just adds one more row and one more column. The technique does not extend to adding an infinite number of constraints (such as adjusting the surface pressure such that a specific sectional load profile is matched or adjusting a surface pressure to match an off-body pressure trace used for sonic boom prediction), but otherwise making adjustments to multidimensional solutions with a finite number of constraints for many problems can be described using this outline. Modest additions, such as matching a line load in a least-squares sense, may enable meeting multidimensional constraints as well.

VI. Summary

This discussion introduced a new analysis technique that enables uncertainty quantification for aerodynamic sectional loads. The method also enables adjustments to the sectional loads to match target integrated forces and moments using a Proper Orthogonal Decomposition and optimization to make the adjustments. By using the POD and data from neighboring sectional load profiles, the adjustments are anchored in plausible realizations and avoid most of the problems with manual or arbitrary adjustments. At its root, this method provides a solution for the problem of adjusting an array of data (for example a one-dimensional sectional load profile or a multidimensional pressure field) to match one or more integrated properties. In essence this technique provides methods to preserve or create consistency. In the example that takes up most of the discussion, this means consistency between a sectional load profile created using computational methods and a force and moment measurement from a wind tunnel experiment, but the main aspects of the technique are applicable to a huge variety of problems.

The sectional load adjustment technique was applied to the aerodynamic sectional loads of NASA's Space Launch System Block 1B crewed vehicle, which is scheduled to be the second or third SLS configuration to launch and will support advanced co-manifested crew and payload exploration missions. Examples are shown for a variety of conditions in the SLS ascent flight conditions including transonic, low supersonic, and maximum dynamic pressure. Plots are shown of nominal loads extracted directly from Computational Fluid Dynamics solutions, adjustments to these loads to match integrated force and moment coefficients measured from a wind tunnel experiment, and dispersed sectional loads that are fully consistent with the uncertainty quantification of the wind tunnel data. By applying these methods to real data from detailed models of flight hardware, the paper demonstrates the capability of the method to support realistic engineering scenarios. Future applications of the new method to launch vehicle aerodynamics will include creating surface pressure databases that are consistent with both sectional loads and integrated forces, base forces from CFD that are consistent with measurements from pressure taps, and the creation of uncertainty quantifications for more data products where it was not previously possible. Finally, these general methods for adjusting data arrays subject to constraints on integral or scalar constraints is likely to have additional applications outside the narrow field of launch vehicle aerodynamics.

Acknowledgments

Resources supporting this work were provided by the NASA High-End Computing Capability (HECC) program through the NASA Advanced Supercomputing (NAS) Division at Ames Research Center. This work was funded by the Space Launch System (SLS) Program.

References

[1] Pandya, S. and Chan, W. M., "Computation of Sectional Loads from Surface Triangulation and Flow Data," *20th AIAA Computational Fluid Dynamics Conference*, 2011, AIAA Paper 2011-3680.

[2] Nichols, R. H., Tramel, R. W., and Buning, P. G., "Solver and Turbulence Model Upgrades to OVERFLOW2 for Unsteady and High-Speed Applications," *36th AIAA Fluid Dynamics Conference*, 2006, AIAA Paper 2006-2824.

[3] Biedron, R. T., Calrson, J., Derlaga, J. M., Gnoffo, P. A., Hammond, D. P., Jones, W. T., Lee-Rausch, E. M., Nielson, E. J., Park, M. A., Rumsey, C. L., Thomas, J. L., and Wood, W. A., "FUN3D Manual: 13.1," Tech. Rep. TM-2017-219580, NASA, 2017.

[4] Chan, W. M., "Advances in Software Tools for Pre-processing and Post-processing of Overset Grid Computations," *Proceedings of the 9th International Conference on Numerical Grid Generation in Computational Field Simulations*, June 2005.

[5] Morris, M. J., Donovan, J. F., Kegelman, J. T., Schwab, S. D., Levy, R. L., and Crites, R. C., "Aerodynamic applications of pressure sensitive paint," *AIAA Journal*, Vol. 31, 1993, pp. 419–425, doi:10.2514/3.11346.

[6] Morris, M. and Lemke, B., "Affordable Pressure-Sensitive Paint Measurements," *41st Aerospace Sciences Meeting and Exhibit*, 2003, AIAA Paper 2003-0092.

[7] Roozeboom, N. and Baerny, J. K., "Customer Guide to Pressure-Sensitive Paint Testing ant NASA Ames Unitary Plan Wind Tunnels," *55th Aerospace Sciences Meeting*, 2017, AIAA Paper 2017-1055.

[8] Hall, K. C., Thomas, J. P., and Dowell, E. H., "Proper Orthogonal Decomposition Technique for Transonic Unsteady Aerodynamic Flows," *AIAA Journal*, Vol. 38, No. 10, 2000, pp. 1853–1862.

[9] Kato, H. and Obayashi, S., "Hybrid Wind Tunnel Based on Ensemble Kalman Filter," *14th International Conference on Information Fusion*, July 2011.

[10] Bauer, S. X. S., Krist, S. E., and Compton, W. B., "Generation of the Ares I-X Flight Test Vehicle Aerodynamic Data Book and Comparison to Flight," *49th AIAA Aerospace Sciences meeting*, 2011, AIAA Paper 2011-11.

[11] Brehm, C., Sozer, E., Moini-Yekta, S., Housman, J. A., Barad, M. F., Kiris, C. C., Vu, B. T., and Parlier, C. R., "Computational Prediction of Pressure Environment in the Flame Trench," *31st AIAA Applied Aerodynamics Conference*, AIAA Paper 2013-2538.

[12] Brehm, C., Housman, J. A., Kiris, C. C., and Hutcheson, F. V., "Noise Characteristics of a Four-Jet Impingement Device Inside a Broadband Engine Noise Simulator," *21st AIAA/CEAS Aeroacoustics Conference*, AIAA Paper 2015-2211.

[13] Rogers, S. E., Dalle, D. J., and Chan, W. M., "CFD Simulations of the Space Launch System Ascent Aerodynamics and Booster Separation," *53rd AIAA Aerospace Sciences Meeting*, January 2015, AIAA Paper 2015-0778.

[14] Barth, T. J., "An Overview of Combined Uncertainty and *A Posteriori* Error Bound Estimates for CFD Calculations," *54th AIAA Aerospace Sciences Meeting*, 2016, AIAA Paper 2016-1062.